



Article

Phase Selectivity in Cr and N Co-Doped TiO₂ Films by Modulated Sputter Growth and Post-Deposition Flash-Lamp-Annealing

Raúl Gago ^{1,*} , Slawomir Prucnal ², René Hübner ², Frans Munnik ² , David Esteban-Mendoza ¹, Ignacio Jiménez ¹ and Javier Palomares ¹

¹ Instituto de Ciencia de Materiales de Madrid, Consejo Superior de Investigaciones Científicas, E-28049 Madrid, Spain

² Helmholtz-Zentrum Dresden-Rossendorf, Institute of Ion Beam Physics and Materials Research, D-01328 Dresden, Germany

* Correspondence: rgago@icmm.csic.es; Tel.: +34-91-334-9090

Received: 11 June 2019; Accepted: 14 July 2019; Published: 17 July 2019



Abstract: In this paper, we report on the phase selectivity in Cr and N co-doped TiO₂ (TiO₂:Cr,N) sputtered films by means of interface engineering. In particular, monolithic TiO₂:Cr,N films produced by continuous growth conditions result in the formation of a mixed-phase oxide with dominant rutile character. On the contrary, modulated growth by starting with a single-phase anatase TiO₂:N buffer layer, can be used to imprint the anatase structure to a subsequent TiO₂:Cr,N layer. The robustness of the process with respect to the growth conditions has also been investigated, especially regarding the maximum Cr content (<5 at.%) for single-phase anatase formation. Furthermore, post-deposition flash-lamp-annealing (FLA) in modulated coatings was used to improve the as-grown anatase TiO₂:Cr,N phase, as well as to induce dopant activation (N substitutional sites) and diffusion. In this way, Cr can be distributed through the whole film thickness from an initial modulated architecture while preserving the structural phase. Hence, the combination of interface engineering and millisecond-range-FLA opens new opportunities for tailoring the structure of TiO₂-based functional materials.

Keywords: oxide materials; doping; sputter deposition; modulated growth; flash-lamp-annealing; XANES

1. Introduction

Titania or titanium dioxide (TiO₂) is a functional wide band-gap semiconductor with tuneable electrical and optical properties by intrinsic (structure in single- or mixed-phase anatase/rutile and/or native defects) or extrinsic (doping) mechanisms [1]. The relevance of doping effects comprises many applications that partially rely on the performance of TiO₂ as a solvent for impurities. In the case of cation dopants, metal incorporation has been used to functionalize or enhance TiO₂ as photocatalyst [2], diluted magnetic semiconductor [3], or transparent conductor material [4].

One of the most interesting properties of TiO₂ relies on its photoactivity, which has been exploited in many applications, such as photocatalysis, hydrogen production, pigments or solar cells [2,5]. However, due to the relatively large band-gap of TiO₂ (>3 eV), its photoactivity is limited to the ultraviolet (UV) region of the solar spectrum (only 5% of the total energy [6]). Therefore, many efforts have been focused on band-gap narrowing for TiO₂ to achieve a visible-light (VISL) response. Such a challenge is mainly realized via doping with foreign atoms at cation or anion sites [2]. In this respect, non-metal (anion) doping has been extensively studied, especially after the work by Asahi et al. [7] on nitrogen (N) doped TiO₂ (TiO₂:N), where the effective optical absorption appears to be related

with intragap localized states [8]. In addition, the solid solubility of N in TiO_2 is rather low, and this situation leads to excess N in (a priori, undesirable) interstitial positions [7]. These sites not only compromise the effectiveness of band-gap narrowing, but provide recombination centres responsible for the loss of photo-generated electron-hole pairs [4]. Metal (cation) doping represents another approach to increase VISL absorption in doped TiO_2 [9], but it induces structural distortions in the host matrix and the defects act as carrier recombination centres [7]. Among these systems, Cr-doped TiO_2 ($\text{TiO}_2\text{:Cr}$) has been addressed due to its catalytic [10,11] and magnetic [12] properties. A recent concept for effective band-gap narrowing relies on simultaneous doping of TiO_2 with anions (C, N, etc.) and transition metals (Cr, V, Mo, etc.). In such a case, the opposite charge states of p- and n-type sites in non-compensated dopants (e.g., Cr/N) should significantly increase the solubility limit of dopant pairs [13]. Based on this hypothesis, Cr–N co-doped TiO_2 ($\text{TiO}_2\text{:Cr,N}$) nanoparticles [6] and single-crystal anatase [14] or rutile [15] thin films have been produced with an extraordinary reduction of the bandgap. The experimental results also indicated that (substitutional) Cr and N dopants are coupled due to the preferential formation of Cr–N bonds [6,14].

In this work, we address the structural impact of co-doping in $\text{TiO}_2\text{:Cr,N}$ films produced by magnetron sputtering. However, Cr containing TiO_2 samples produced by this method typically have a poor crystalline quality even under growth on heated substrates up to 500 °C [16]. This eventual drawback represents a handicap with respect to other methods producing $\text{TiO}_2\text{:Cr,N}$ films with high structural quality [13,14]. Post-deposition treatments can be used to enhance the structural quality where, additionally, further dopant activation or the promotion of a specific structure can be achieved. For industry-oriented applications, non-contact and rapid treatments pose a great advantage. Among such methods, millisecond-range flash-lamp-annealing (FLA) [8] enables the control of dopant diffusion and activation, where only the near-surface region is annealed and rapidly cooled. Recently, we reported [17] the structural impact of Cr incorporation before and after FLA in TiO_2 films grown by magnetron sputtering. We found that TiO_2 phases can accommodate up to ~5 at.% Cr and, in general, rutile environments are favored. This situation may not be desirable for certain applications, since the anatase phase shows a substantially higher photoactivity than rutile [18]. However, phase selectivity in TiO_2 -based films is a complex competition between nucleation and growth mechanisms. Rutile is the most stable and dense structure, whereas anatase is a metastable phase. The nucleation of rutile requires more energy input than anatase, but after nucleation it grows more easily within a wider range of conditions than anatase [19].

The objectives of this work are two-fold. First, we aim to extend our previous structural study to co-doped films. Second, we seek growth or processing conditions that yield preferential formation of the anatase phase. Since, as stated above, the growth regime for anatase seems to be the limiting factor, we test the preparation of modulated architectures as an attempt to transfer and retain the growth of the anatase phase in the Cr-containing layer. Remarkably, this approach has been found to be rather successful. In addition, FLA has been used to improve the quality of the resulting phase and to induce dopant activation and diffusion. The present results provide a relevant framework for tailoring the atomic structure of TiO_2 -based mixed oxides by exploiting the concept of interface engineering in combination with FLA.

2. Materials and Methods

2.1. Sample Preparation

In this work, $\text{TiO}_2\text{:Cr,N}$ coatings were grown by reactive magnetron sputtering on p-type (B doped) commercial Si(100) substrates (University Wafer, South Boston, MA, USA) cleaved into $12 \times 12 \text{ mm}^2$ pieces. Individual 3" Ti and Cr targets (99.99% purity, Testbourne Ltd., Basingstoke, UK) were used for co-sputtering, both located at ~15 cm from the grounded substrates in a confocal geometry at an angle of 30° with respect to the substrate normal. The base pressure in the deposition chamber was 10^{-4} Pa. The working pressure was 0.5 Pa with a gas (99.9995% purity grade) mixture of Ar (50%), N_2

(44%) and O₂ (6%) set by individual mass flow controllers. For plasma generation, a DC signal with a power of 150 W was applied to the Ti cathode, whereas the power applied to the Cr cathode, W_{Cr} , was modulated from 0 to 25 W according to the desired coating architecture. In all cases, the growth was carried out for 2 h, resulting in a total thickness of ~100 nm. Monolithic and modulated film architectures were studied. In the first case, W_{Cr} was kept constant during the whole deposition time. In the latter case, a buffer TiO₂:N films was initially grown ($W_{Cr} = 0$ W) with a thickness up to several tens of nm's followed by the subsequent instant (bilayer coating) or gradual (gradient coating) increase in W_{Cr} to produce the Cr-containing layer(s). The deposition was done at a substrate temperature, T_s , of 300 °C to achieve high-quality anatase phase in TiO₂:N films [20].

The as-grown samples were cut in two and one piece was kept as a reference while the other was processed with FLA for 20 ms at a continuous flow of N₂ (99.999% purity). The overall energy density was set to ~70 J/cm² according to the optimum conditions for anatase crystallization from (amorphous) pure TiO₂ films [17]. Such FLA condition corresponds to a maximum surface temperature in the range of 1100 °C. The heating and cooling rate during millisecond FLA is in the range of 100 K/ms and 200 K/s, respectively. Further details about the FLA system can be found in [21].

2.2. Sample Characterization

The composition profile of the TiO₂:Cr,N layers was determined by Rutherford backscattering spectrometry (RBS). The measurements were performed at the Ion Beam Center (IBC) of Helmholtz-Zentrum Dresden-Rossendorf (HZDR) using a 1.7 MeV He⁺ probing beam. The RBS spectra were acquired under normal incidence with a “random” scan (to avoid channelling effects in the substrate signal), and the backscattered particles were detected with a silicon detector at a scattering angle of 165°. For quantitative analysis, the RBS spectra were simulated with the SIMNRA code [22]. Complementary compositional analysis regarding light elements was done by means of heavy-ion elastic recoil detection analysis (ERDA). The measurements were carried out with a 35 MeV Cl⁷⁺ beam impinging at 75° with respect to the sample surface normal. The scattered ions and recoils were detected with a Bragg ionization chamber (BIC) located at a scattering angle of 31°. The BIC chamber allows for the discrimination of detected particles according to their atomic number (Z). The analysis of the recoil spectra and scattered Cl spectrum was performed simultaneously for each sample with the code NDF [23].

The phase structure of the samples was examined by grazing-incidence X-ray diffraction (GI-XRD) measurements using a D5000 (BRUKER AXS, Billerica, MA, USA) diffractometer with Cu-K α radiation (wavelength of 1.5418 Å). The data were collected at an incidence angle of 0.5°. The local bonding structure with element sensitivity was studied by X-ray absorption near-edge structure (XANES) analysis [24] with soft X-rays. XANES provides short-range information of electronic states for each individual element, being a powerful technique to study complex multi-element systems. Moreover, the technique can be applied to materials with either amorphous or crystalline structure. Particularly, TiO₂-based materials have been widely studied by XANES, providing clear distinct spectral fingerprints of TiO₂ polymorphs that can be used for univocal phase identification [25]. XANES measurements were carried out at the dipole beamline PM3 of the synchrotron facility BESSY-II of Helmholtz-Zentrum Berlin (HZB). The data were acquired using the ALICE endstation in the total electron yield (TEY) mode. TEY-XANES probes the near-surface region (up to a few tens of nm's) and, therefore, in-depth structural information can be achieved by the combination of XANES and XRD. The electronic structure has also been studied by high-resolution X-ray photoelectron spectroscopy (XPS). The spectra were acquired with a Phoibos 150 spectrometer (SPECS, Berlin, Germany) equipped with a hemispherical analyser and 2D-DLD detector. The measurements were performed with monochromatic Al K α radiation at normal emission take-off angle. The spectra were acquired using an energy step of 0.05 eV and pass-energy of 10 eV, providing an overall instrumental peak broadening of ~0.4 eV.

The microstructure of the TiO₂:Cr,N thin films was analysed locally with cross-sectional transmission electron microscopy (TEM) using an image C_s-corrected Titan 80–300 microscope

(FEI, Eindhoven, Netherlands) operated at an accelerating voltage of 300 kV. TEM specimens were prepared by sawing, grinding, dimpling, and finally, Ar^+ ion-milling. In particular, bright-field TEM imaging and selected-area electron diffraction (SAED) were performed. Since the smallest available selected area aperture of 10 μm covers a circular area with a diameter of about 190 nm, amorphous glue used for TEM specimen preparation contributes to the SAED patterns recorded. Complementary information was extracted from high-angle annular dark-field scanning transmission electron microscopy (HAADF-STEM) imaging and spectrum imaging analysis based on energy-dispersive X-ray spectroscopy (EDXS). This analysis was performed with a Talos F200X microscope (FEI, Brno, Czech Republic) operated at 200 kV and equipped with a Super-X EDXS detector system. The TEM specimens were placed for 8 s into a Model 1020 Plasma Cleaner (Fischione, Export, PA, USA) to remove organic surface contamination before the analysis.

3. Results and Discussion

3.1. Compositional Profile in Monolithic and Modulated Films

Figure 1 shows the experimental (dots) and fitted (solid lines) RBS data from monolithic and modulated $\text{TiO}_2\text{:Cr,N}$ coatings. In this case, the monolithic film was produced with constant power $W_{\text{Cr}} = 15 \text{ W}$ during the whole deposition time. The bilayer coating was produced with $W_{\text{Cr}} = 0 \text{ W}$ for one half of the deposition time ($\sim 50 \text{ nm}$), followed by switching on the discharge on the Cr cathode to $W_{\text{Cr}} = 15 \text{ W}$ during the rest of the process. Finally, the gradient coating was produced with $W_{\text{Cr}} = 0 \text{ W}$ for one fourth of the total deposition time ($\sim 25 \text{ nm}$) and a stepwise increase of W_{Cr} by 5 W each 30 min. The designed layer structures for the different coating architectures are depicted as inset in Figure 1. The contributions from the various elements to the overall RBS spectra are also labelled in the figure. The Cr contribution to the overall spectra obtained from the fitting results is also included in the graph and reflects the different layer arrangements. Moreover, the Cr doping level is similar ($\sim 4 \text{ at.}\%$) at the near surface region for all cases (where $W_{\text{Cr}} = 15 \text{ W}$), with a Cr/Ti ratio of around 0.15. Obviously, the Cr concentration is constant for the whole film thickness in the monolithic film. The RBS cross-section is low for light elements and, hence, only the oxygen signal is clearly detected due to its large concentration. However, the N content is found to be around 2–3 at.%, as derived by complementary ERDA measurements.

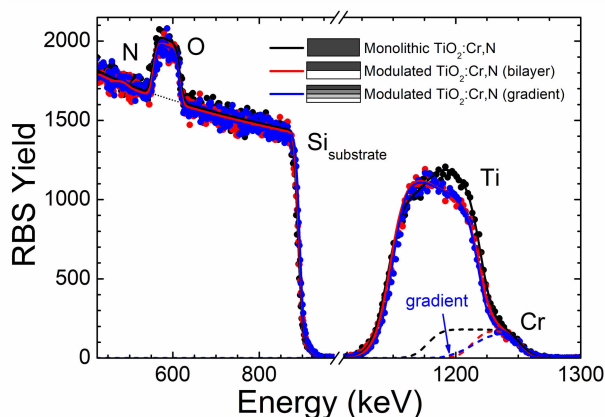


Figure 1. RBS (Rutherford backscattering spectrometry) data (dots) and fitted spectra (solid lines) for as-grown $\text{TiO}_2\text{:Cr,N}$ coatings grown on Si(100) substrates with monolithic and modulated (bilayer and gradient architectures) structures. The individual element contribution from Cr to the fitted spectra is also shown (dotted lines).

3.2. Structural Investigations of Monolithic and Modulated Films

Figure 2 shows the GI-XRD patterns from monolithic and modulated $\text{TiO}_2\text{:Cr,N}$ coatings as well as from TiO_2 and $\text{TiO}_2\text{:N}$ monolithic films grown under equivalent conditions. The TiO_2 coating shows a mixture of rutile and anatase phases for this particular growth condition, although the relative phase contribution can be tuned, among other parameters, by the oxygen partial pressure [26]. Note that the broad bump around 55° comes from the underlying Si(100) substrate. The dominant A_{101} reflection from the $\text{TiO}_2\text{:N}$ coating evidences that the addition of N under these conditions prevents rutile formation and yields a nearly single-phase anatase film. This effect was reported in detail in a previous publication by some of the present authors [20] and other groups [27–29]. In the Cr co-doped monolithic film, the structure displays a strong mixed-phase character where the rutile content is significantly higher than in the pure TiO_2 film. As discussed in the introduction, this result supports the favourable formation of rutile environments upon Cr incorporation. The R_{110} reflection from rutile in the monolithic $\text{TiO}_2\text{:Cr,N}$ coating is considerably broad, which can be attributed to both the structural disorder induced by Cr incorporation into the oxide matrix and, eventually, the formation of a rutile hybrid oxide in a similar fashion as observed in Cr-doped TiO_2 [17]. Remarkably, the anatase selectivity in the $\text{TiO}_2\text{:N}$ buffer layer can be effectively used to imprint this structural phase to the co-doped layer in the modulated growth. Indeed, both modulated films display strong A_{101} Bragg reflections corresponding to a nearly single-phase structure. The similar result in both modulated designs supports the validity of the transfer process, where anatase keeps on growing by either increasing the Cr content progressively or abruptly. The widths of the A_{101} Bragg reflection indicate that the anatase phase is nanocrystalline, with grain sizes of around 20 nm, as estimated by the Scherrer formula [30]. Finally, in all Cr-containing films, no evidence of Cr–O phase segregation is observed.

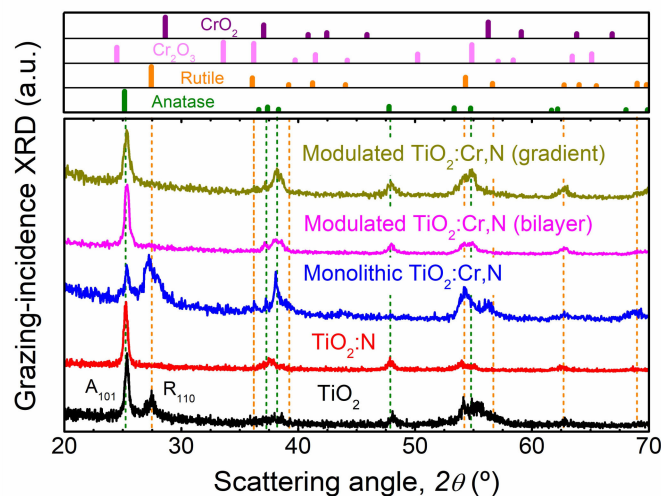


Figure 2. Grazing-incidence XRD patterns from TiO_2 , $\text{TiO}_2\text{:N}$ and $\text{TiO}_2\text{:Cr,N}$ (monolithic/modulated) coatings grown under equivalent conditions. The diffraction patterns from anatase (PDF-00-021-1272), rutile (PDF-00-021-1276), Cr_2O_3 (PDF-00-001-0622) and CrO_2 (PDF-00-001-0622) reference compounds are shown in the upper panel for phase identification.

For complementary phase identification at the near-surface region, the bonding structure around host and dopant sites has been studied in detail by XANES. The spectra for the Ti 2p, O 1s, Cr 2p and N 1s element edges are shown in Figure 3. For the sake of clarity, only the spectra from the bilayer coating are shown as representative case of the modulated growth (same results were obtained from the gradient design). The element spectra from corresponding reference binary oxides as extracted from the literature are also shown for comparison. In particular, the TiO_2 references refer to the spectra reported for polycrystalline films by Ruus et al. [31]. Regarding chromium oxides, we have included the

spectra from single-crystal Cr_2O_3 [32], CrO_2 deposited film [33] and CrO_3 powder [34]. Accordingly, the spectral features from the latter oxides can be used as fingerprints of environments with oxidation state Cr^{3+} , Cr^{4+} and Cr^{6+} , respectively. Basically, the individual XANES spectra can be interpreted as a picture of the density of Ti-3d , O-2p , N-2p , and Cr-3d states according to dipole selection rules. A detailed description of the origin of the different spectral features and regions can be found in previous publications for binary [26,35] and ternary [17,20] oxides. The most direct information about the oxide matrix can be found in the $\text{Ti } 2p$ edge, where anatase and rutile TiO_2 display clear distinct features, especially in the double-peak structure within the 459–462 eV region. In this way, the $\text{Ti } 2p$ line shape indicates a dominant rutile and anatase structure for monolithic and modulated films, respectively. Then, surface-sensitive XANES results prove that the anatase phase in the $\text{TiO}_2:\text{N}$ buffer layer is clearly transferred from the interface up to the surface in the Cr-containing layer by the modulated growth.

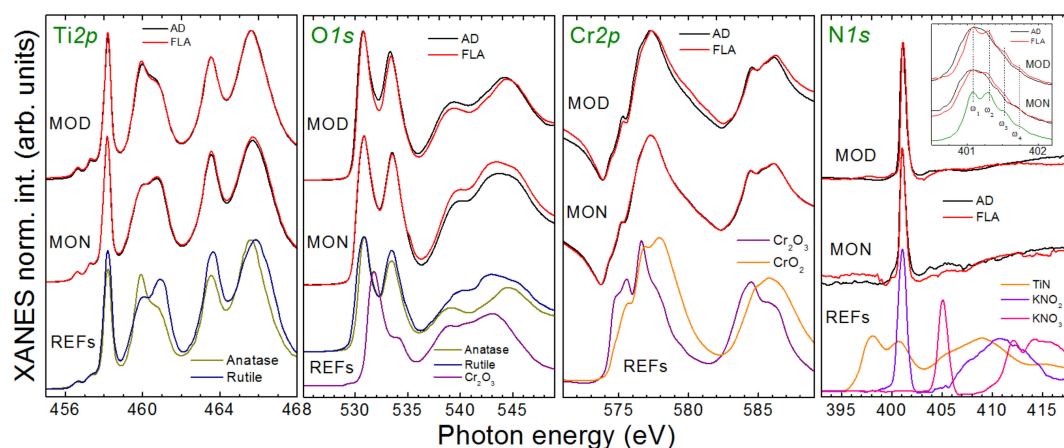


Figure 3. XANES spectra at the different element edges for monolithic (MON) and modulated (MOD) $\text{TiO}_2:\text{Cr,N}$ coatings before (black) and after (red) FLA. The reference spectra from binary oxide compounds are also included in the bottom part (see text for details).

The $\text{O } 1s$ leads to similar conclusions in relation to the dominant titania phase. Moreover, there is no evidence of O-Cr bonds, since the signal is dominated by the TiO_2 matrix. In any case, information about the Cr sites can be extracted from the $\text{Cr } 2p$ edge. The $\text{Cr } 2p$ spectra are rather broad in comparison to the reference oxides due to the nanocrystalline nature of the films. The spectra show a marked background since the $\text{Cr } 2p$ edge is superimposed to the $\text{O } 1s$ post-edge and, in addition, the Cr content in the films is relatively low. Here, the adsorption onset and spectral features indicate that most of the Cr dopants are in the Cr^{3+} oxidation state [17,35]. This situation has been considered as an indication of the substitutional nature of Cr dopants [6] and, from a practical point of view, can also be relevant to improve the photocatalytic response [10,11]. However, a certain contribution from Cr^{4+} (CrO_2) may also be plausible by the increased intensity in the 578–579 and 586–588 eV regions. The presence of Cr^{4+} sites could also be correlated with the formation of a (secondary) mixed-oxide rutile phase [17], as suggested by the rather broad R_{110} Bragg reflection in the GI-XRD pattern from the monolithic $\text{TiO}_2:\text{Cr,N}$ in Figure 2. Regarding N sites, the XANES $\text{N } 1s$ shows a main contribution of interstitial sites in the form of $-\text{NO}_x$ radicals ($x \sim 2$), as evidenced by the intense peak at ~ 401 eV. However, as shown for the case of N-doped TiO_2 [26], such environments may have a relatively large cross-section and some N can also be in substitutional sites (N–Ti). This is further discussed below when presenting the XPS results.

3.3. Effect of Flash-Lamp-Annealing (FLA)

The impact of FLA on the structural properties of monolithic and modulated films was also examined. XANES spectra of the flashed (red curves) and as-deposited (black curves) films are

compared in Figure 3. Since the films were grown at moderate temperatures, the modifications induced by FLA are not severe. However, there are subtle changes that are worth mentioning. First, the low energy peak at ~ 461 eV is promoted and sharpened at the Ti 2p edge of the modulated film, which evidences a slight increase in the quality of the anatase phase. A similar structural improvement is hinted in the rutile features for the monolithic film. Another relevant change induced by FLA in both structures is related to the nature of N environments. In particular, the high-resolution scan of the N 1s peak around 401 eV (see inset) reveals the appearance of a fine structure, a fingerprint of the formation of N_2 molecules inside the oxide matrix [20].

The structural changes induced by FLA were also studied by GI-XRD (note that this analysis was performed in smaller samples than those in Figure 2). In agreement with XANES, the XRD patterns in Figure 4 also show that the phase composition is not significantly altered by FLA. In this case, a small transformation into rutile takes place in the bilayer coating, which is not observed for the case of a gradient profile. In addition, the A_{101} Bragg peak in modulated coatings displays a shift after FLA to higher angles (smaller lattice parameter). This should be mainly attributed to strain effects, but another plausible contribution could be the promotion of N substitutional sites (see below).

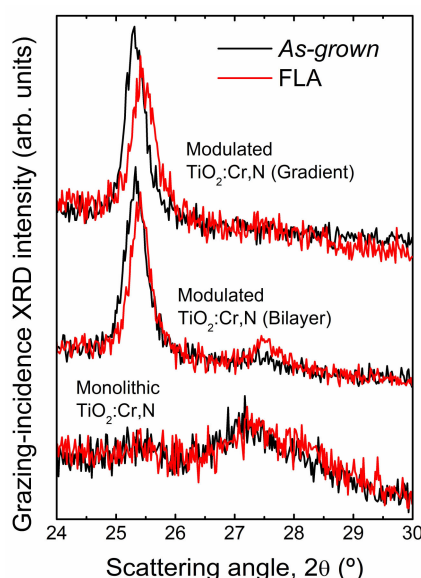


Figure 4. Grazing-incidence XRD patterns from monolithic and modulated $TiO_2:Cr,N$ coatings before and after FLA. The anatase phase in modulated coatings shows a shift to higher scattering angles (lattice contraction) with the thermal treatment.

In order to deepen in the evolution of N environments, XPS was performed in as-deposited and FLA samples. The N 1s core-level spectra for the different samples are shown in Figure 5. In line with the XANES, XPS of as-grown samples shows the dominance of interstitial sites (N–O), together with the presence of N_2 molecules (N–N). Note that FLA increases the relative contribution of N–N bonds, as already pointed out by XANES. Remarkably, FLA also transforms N into substitutional sites (Ti–N) and, hence, it clearly favors activation of the anion dopant.

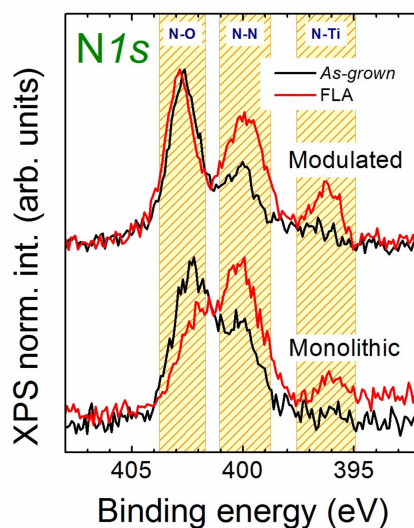


Figure 5. N 1s core-level spectra from monolithic and modulated $\text{TiO}_2\text{:Cr,N}$ coatings before and after FLA.

The impact of FLA on the film morphology and phase structure was also studied by TEM analysis. Figure 6 shows cross-sectional bright-field TEM images of the monolithic and modulated architecture with a gradient profile. In both samples, there is a thin (~ 2 nm) SiO_2 layer at the substrate-coating interface coming from the native oxide of the Si(100) wafers. The images show columnar grain growth with in-plane diameters of a few tens of nanometres, which is consistent with the grain size estimated by GI-XRD. Irrespective of the film architecture, the crystal growth is more or less homogenous across the whole layer thickness. The samples after FLA show a more pronounced grain orientation contrast close to the interface to the substrate, which can be correlated with an enhanced crystallinity in that region. The presence of pores in the early stage of growth can also be seen in both samples, although they are more evident in the $\text{TiO}_2\text{:N}$ buffer layer within the modulated design. Such pore structures can be resolved more clearly in slightly under-focused (UF) bright-field TEM images, as shown in Figure 6 from a magnified view of the film-substrate interface region. It is also relevant that those structures increase in size after FLA. The UF images also emphasize the enhancement (darker zones) of the film crystalline quality near the substrate interface after FLA. Finally, selected-area electron diffraction (SAED) analysis shown in Figure 6 from the imaged regions supports the phase formation derived from XANES and XRD, with a dominant rutile or anatase character for monolithic and modulated coatings, respectively.

Spectrum imaging analysis based on EDXS was done at the cross-sectional TEM specimens to study the in-depth element distributions. The corresponding HAADF-STEM micrographs and the EDXS element maps are shown in Figure 7. The images reveal homogenous distributions of Ti, O and N atoms. Note that there is also an additional narrow N contribution below the native oxide layer, which should be attributed to the commercial wafer fabrication process. The Cr distributions from the as-deposited samples clearly reproduce the coating designs, where the different interfaces resulting from the modulated growth can be identified, as highlighted by the dashed lines in the figure. The preservation of the expected profile also evidences that TEM specimen preparation has not altered the element distributions. Interestingly, the Cr distribution obtained after FLA in the modulated structure shows that the thermal treatment can (at least partially) homogenize the initial Cr profile. Therefore, one could design a modulated structure for phase selectivity and subsequently distribute the Cr dopants by FLA. Quantitative EDXS analysis (line scans not shown here) provide similar results as RBS and ERD with Cr and N contents of a few at.%. In the monolithic film, there is a slight accumulation of N in the region where the aforementioned pores are observed (note the contrast in this region in the HAADF-STEM images due to the reduced atomic number). Therefore, we

assume that such mesoporous structure may be filled with N_2 (bubbles). Note that the promotion of N_2 after FLA has been detected at the near-surface region by XANES and XPS. In this regard, it should be mentioned that the reduced N signal in the pore region for the FLA-treated modulated film (see Figure 7) is most probably caused by N_2 release from the enlarged and interconnected pores, which get opened during preparation of the thin electron-transparent TEM lamella.

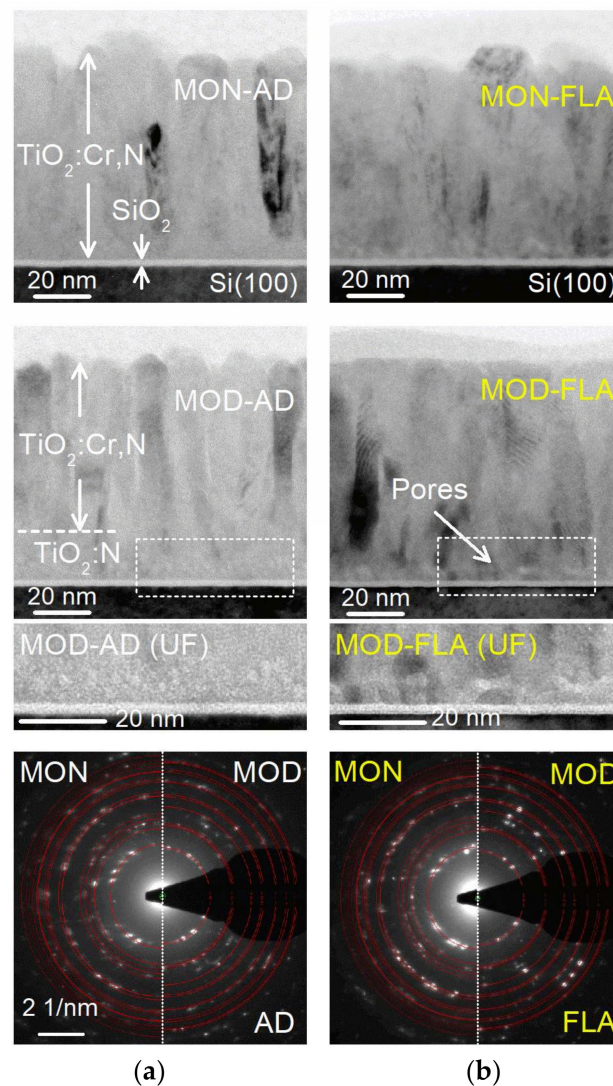


Figure 6. Cross-sectional bright-field TEM images from monolithic (MON) and modulated (MOD) $TiO_2:Cr,N$ coatings as-deposited (AD) (a) and after FLA (b). The slightly under-focused (UF) bright-field images in the third row are magnified views of the marked regions close to the substrate-coating interface in the MOD case to enhance the contrast of the pore structures. Corresponding representative SAED patterns displayed in the bottom part confirm the dominant rutile and anatase character for MON and MOD coatings, respectively.

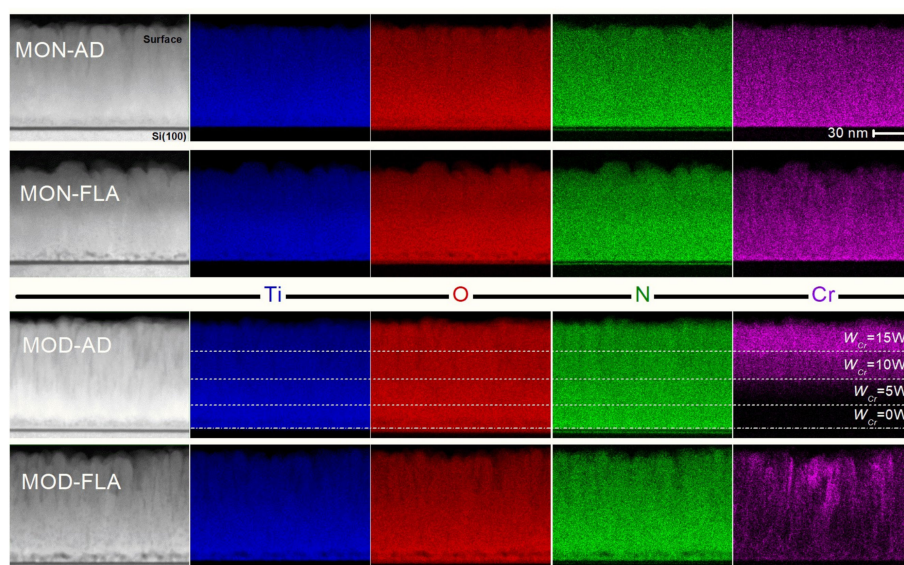


Figure 7. HAADF-STEM micrographs and element distributions obtained by EDXS analysis of monolithic (MON) and modulated (MOD) coatings in as-deposited (AD) and after FLA states. Dashed lines in the MOD-AD coating indicate the interfaces caused by the gradient steps during film growth.

3.4. Final Remarks

One relevant question regarding the modulated growth relies on the generalization of the phase selectivity for other growth conditions and coating designs. For this purpose, additional processing windows were tested. First, higher W_{Cr} were sampled for the stability of the anatase phase against higher Cr contents in the films. In particular, bilayer films were produced with W_{Cr} up to 25 W in the second growth stage. This change implies a slight increase of the Cr content from ~4 to ~5 at.%, as extracted from RBS. As shown in the Ti 2p XANES spectra in Figure 8, the progressive increase in Cr results in a higher promotion of the rutile phase. Hence, single-phase anatase $TiO_2:Cr,N$ layers produced in modulated structures can only accommodate Cr contents below the threshold of ~5 at.%. Interestingly, the Ti 2p spectra from the samples after FLA (red curves) confirm that the thermal treatment improves the crystal structure, and even restores the anatase dominance for the highest Cr contents. The latter could be related to the aforementioned redistribution of Cr after FLA, which would imply an effective decrease in the Cr content. Such a hypothesis is supported by the relative intensity of the corresponding XANES edges (not shown).

Another crucial parameter in the modulated growth is the substrate temperature. As indicated in the experimental section, we selected the lowest temperature (300 °C) capable of producing high-quality anatase $TiO_2:N$ layer [20] for the buffer layer. This means that we could obtain better (worse) quality anatase phase at higher (lower) temperatures. The thickness of the Cr-containing layer should also be considered to test how long the anatase growth can be sustained in the modulated mode. To study this influence, we prepared bilayer coatings by increasing the Cr-containing layer from 50 to 75 nm. In the latter case, the structure preserves the anatase character, but the rutile contribution starts to increase for the thicker layer.

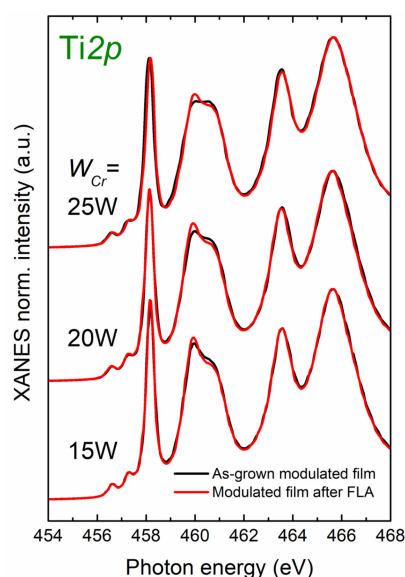


Figure 8. XANES spectra of modulated films with a bilayer structure produced with different W_{Cr} in the uppermost layer in as-grown (black curves) and after FLA (red curves) states.

Finally, in the present work, we have focused our investigations on the structural properties related to the modulated growth. Obviously, additional efforts should be devoted to varying the FLA conditions and modulated designs in order to optimize the structural quality. In addition, a natural continuation of this work would be testing the performance of these coatings for photocatalytic applications.

4. Conclusions

In conclusion, we have studied the phase formation in $TiO_2:Cr,N$ thin films and exploited interface engineering concepts for phase selectivity. In particular, monolithic coatings result in the formation of a mixed-phase oxide with dominant rutile character. Remarkably, under equivalent conditions, the favourable formation of single-phase anatase in a $TiO_2:N$ buffer layer can be utilized to transfer this structure into $TiO_2:Cr,N$. Such phase selectivity in the Cr-containing film occurs in both gradual and abrupt Cr profiles. However, the production of single-phase anatase seems to be limited to low Cr contents (<5 at.%) and is less effective as the film thickness is increased. Post-deposition millisecond-range FLA was used to enhance the quality of the as-grown phase together with dopant activation and diffusion. This work shows that the combination of modulated growth designs and FLA opens new opportunities for tailoring the desired structure of TiO_2 -based materials.

Author Contributions: Conceptualization, R.G. and S.P.; Methodology, R.G. and S.P.; Validation, R.G., S.P., and R.H.; Formal Analysis, R.G., S.P., R.H. and F.M.; Investigation, R.G., S.P., R.H., F.M., D.E.-M., I.J. and J.P.; Resources, R.G., S.P., R.H., F.M. and J.P.; Writing—Original Draft Preparation, R.G.; Writing—Review and Editing, R.G., S.P., R.H., F.M., D.E.-M., I.J. and J.P.; Visualization, R.G. and R.H.; Supervision, R.G. and S.P.; Project Administration, R.G. and S.P.; Funding Acquisition, R.G., S.P., R.H., I.J., and J.P.

Funding: The research leading to these results has received funding from projects RTI2018-095137-B-I00 and MAT2016-80394-R from *Ministerio de Ciencia, Innovación y Universidades* (Spain) and grant agreement n° 226716 from the European Community's Seventh Framework Programme (FP7/2007-2013). Funding of TEM Talos F200X by the German Federal Ministry of Education of Research (BMBF) through Grant No. 03SF0451 in the framework of HEMCP is gratefully acknowledged.

Acknowledgments: We thank HZB and HZDR for the allocation of beamtime for the synchrotron and ion beam analysis experiments, respectively. Support by the TEM facilities at IBC-HZDR is gratefully acknowledged. The authors would also like to thank R. Aniol at HZDR for TEM specimen preparation.

Conflicts of Interest: The authors declare no conflict of interest.

References

- Diebold, U. The surface science of titanium dioxide. *Surf. Sci. Rep.* **2003**, *48*, 53–229. [[CrossRef](#)]
- Henderson, M.A. A surface science perspective on TiO₂ photocatalysis. *Surf. Sci. Rep.* **2011**, *66*, 185–297. [[CrossRef](#)]
- Matsumoto, Y.; Murakami, M.; Shono, T.; Hasegawa, T.; Fukumura, T.; Kawasaki, M.; Ahmet, P.; Chikyow, T.; Koshihara, S.; Koinuma, H. Room-temperature ferromagnetism in transparent transition metal-doped titanium dioxide. *Science* **2001**, *291*, 854–856. [[CrossRef](#)] [[PubMed](#)]
- Serpone, N. Is the band gap of pristine TiO₂ narrowed by anion- and cation-doping of titanium dioxide in second-generation photocatalysts? *J. Phys. Chem. B* **2006**, *110*, 24287–24293. [[CrossRef](#)] [[PubMed](#)]
- Vitiello, G.; Pezzella, A.; Calcagno, V.; Silvestri, B.; Raiola, L.; D’Errico, G.; Costantini, A.; Branda, F.; Luciani, G. 5,6-Dihydroxyindole-2-carboxylic acid–TiO₂ charge transfer complexes in the radical polymerization of melanogenic precursor(s). *J. Phys. Chem. C* **2016**, *120*, 6262–6268. [[CrossRef](#)]
- Chiodi, M.; Cheney, C.P.; Vilmercati, P.; Cavaliere, E.; Mannella, N.; Weitering, H.H.; Gavioli, L. Enhanced dopant solubility and visible-light absorption in Cr–N codoped TiO₂ nanoclusters. *J. Phys. Chem. C* **2012**, *116*, 311–318. [[CrossRef](#)]
- Asahi, R.; Morikawa, T.; Ohwaki, T.; Aoki, K.; Taga, Y. Visible-light photocatalysis in nitrogen-doped titanium oxides. *Science* **2001**, *293*, 269–271. [[CrossRef](#)]
- Batzill, M.; Morales, E.H.; Diebold, U. Influence of nitrogen doping on the defect formation and surface properties of TiO₂ rutile and anatase. *Phys. Rev. Lett.* **2006**, *96*, 026103. [[CrossRef](#)]
- Clarizia, L.; Vitiello, G.; Pallotti, D.K.; Silvestri, B.; Nadagouda, M.; Lettieri, S.; Luciani, G.; Andreozzi, R.; Maddalena, P.; Marotta, R. Effect of surface properties of copper-modified commercial titanium dioxide photocatalysts on hydrogen production through photoreforming of alcohols. *Int. J. Hydrogen Energy* **2017**, *42*, 28349–28362. [[CrossRef](#)]
- Zhu, J.; Deng, Z.; Chen, F.; Zhang, J.; Chen, H.; Anpo, M.; Huang, J.; Zhang, L. Hydrothermal doping method for preparation of Cr³⁺–TiO₂ photocatalysts with concentration gradient distribution of Cr³⁺. *Appl. Catal. B: Environ.* **2006**, *62*, 329–335. [[CrossRef](#)]
- Fan, X.; Chen, X.; Zhu, S.; Li, Z.; Yu, T.; Ye, J.; Zou, Z. The structural, physical and photocatalytic properties of the mesoporous Cr-doped TiO₂. *J. Mol. Catal. A Chem.* **2008**, *284*, 155–160. [[CrossRef](#)]
- Kaspar, T.C.; Heald, S.M.; Wang, C.M.; Bryan, J.D.; Droubay, T.; Shutthanandan, V.; Thevuthasan, S.; McCready, D.E.; Kellock, A.J.; Gamelin, D.R.; et al. Negligible magnetism in excellent structural quality Cr_xTi_{1–x}O₂ anatase: contrast with high-T_C ferromagnetism in structurally defective Cr_xTi_{1–x}O₂. *Phys. Rev. Lett.* **2005**, *95*, 217203. [[CrossRef](#)] [[PubMed](#)]
- Zhu, W.; Qiu, X.; Iancu, V.; Chen, X.Q.; Pan, H.; Wang, W.; Dimitrijevic, M.N.; Rajh, T.; Meyer, H.M.; Paranthaman, M.P.; et al. Band gap narrowing of titanium oxide semiconductors by noncompensated anion-cation codoping for enhanced visible-light photoactivity. *Phys. Rev. Lett.* **2009**, *103*, 226401. [[CrossRef](#)] [[PubMed](#)]
- Wang, Y.; Cheng, Z.; Tan, S.; Shao, X.; Wang, B.; Hou, J.G. Characterization of Cr–N codoped anatase TiO₂(001) thin films epitaxially grown on SrTiO₃(001) substrate. *Surf. Sci.* **2013**, *616*, 93. [[CrossRef](#)]
- Cheng, Z.; Zhang, L.; Dong, S.; Ma, X.; Ju, H.; Zhu, J.; Cui, X.; Zhao, J.; Wang, B. Electronic properties of Cr–N codoped rutile TiO₂(110) thin films. *Surf. Sci.* **2017**, *666*, 84–89. [[CrossRef](#)]
- Kollbek, K.; Szkudlarek, A.; Marzec, M.M.; Lyson-Sypien, B.; Cecot, M.; Bernasik, A.; Radecka, M.; Zakrzewska, K. Optical and electrical properties of Ti(Cr)O₂:N thin films deposited by magnetron co-sputtering. *Appl. Surf. Sci.* **2016**, *380*, 73–82. [[CrossRef](#)]
- Gago, R.; Prucnal, S.; Pérez-Casero, R.; Caretti, I.; Jiménez, I.; Lungwitz, F.; Cornelius, S. Structural impact of chromium incorporation in as-grown and flash-lamp-annealed sputter deposited titanium oxide films. *J. Alloy Compd.* **2017**, *729*, 438–445. [[CrossRef](#)]
- Xu, M.; Gao, Y.; Martinez-Moreno, E.; Kunst, M.; Muhler, M.; Wang, Y.; Idriss, H.; Wöll, C. Photocatalytic activity of bulk TiO₂ anatase and rutile single crystals using infrared absorption spectroscopy. *Phys. Rev. Lett.* **2011**, *106*, 138302. [[CrossRef](#)]
- Houska, J.; Mraz, S.; Schneider, J.M. Experimental and molecular dynamics study of the growth of crystalline TiO₂. *J. Appl. Phys.* **2012**, *112*, 073527. [[CrossRef](#)]

20. Gago, R.; Redondo-Cubero, A.; Vinnichenko, M.; Lehmann, J.; Munnik, F.; Palomares, F.J. Spectroscopic evidence of NO_x formation and band-gap narrowing in N-doped TiO₂ films grown by pulsed magnetron sputtering. *Mater. Chem. Phys.* **2012**, *136*, 729–736. [[CrossRef](#)]
21. Skorupa, W.; Gebel, T.; Yankov, R.A.; Paul, S.; Lerch, W.; Downey, D.F.; Arevalo, E.A. Advanced thermal processing of ultrashallow implanted junctions using flash lamp annealing. *J. Electrochem. Soc.* **2005**, *152*, G436–G440. [[CrossRef](#)]
22. Mayer, M. *SIMNRA User's Guide 6.05*; Max-Planck-Institut für Plasmaphysik: Garching, Germany, 2009.
23. Barradas, N.P.; Jeynes, C.; Webb, R.P. Simulated annealing analysis of Rutherford backscattering data. *Appl. Phys. Lett.* **1997**, *71*, 291–293. [[CrossRef](#)]
24. Stöhr, J. *NEXAFS Spectroscopy*; Springer: New York, NY, USA, 1992.
25. Crocombette, J.P.; Jollet, F. Ti 2p X-ray absorption in titanium dioxides (TiO₂): The influence of the cation site environment. *J. Phys. Condens. Matter* **1994**, *6*, 10811. [[CrossRef](#)]
26. Gago, R.; Vinnichenko, M.; Redondo-Cubero, A.; Czigány, Z.; Vázquez, L. Surface morphology of heterogeneous nanocrystalline rutile/amorphous anatase TiO₂ films grown by reactive pulsed magnetron sputtering. *Plasma Process. Polym.* **2010**, *7*, 813–823. [[CrossRef](#)]
27. Lindgren, T.; Mwabora, J.M.; Avendano, E.; Jonsson, J.; Hoel, A.; Granqvist, C.G.; Lindquist, S. Photoelectrochemical and optical properties of nitrogen doped titanium dioxide films prepared by reactive DC magnetron sputtering. *J. Phys. Chem. B* **2003**, *107*, 5709–5716. [[CrossRef](#)]
28. Madhavi, V.; Kondaiah, P.; Mohan Rao, G. Influence of silver nanoparticles on titanium oxide and nitrogen doped titanium oxide thin films for sun light photocatalysis. *Appl. Surf. Sci.* **2018**, *436*, 708–719.
29. Mwabora, J.M.; Lindgren, T.; Avendaño, E.; Jaramillo, T.F.; Lu, J.; Lindquist, S.E.; Granqvist, C.G. Structure, composition, and morphology of photoelectrochemically active TiO_{2-x}N_x thin films deposited by reactive DC magnetron sputtering. *J. Phys. Chem. B* **2004**, *108*, 20193–20198. [[CrossRef](#)]
30. Klug, H.P.; Alexander, L.E. *X-ray Diffraction Procedures for Polycrystalline and Amorphous Materials*; Wiley: Hoboken, NJ, USA, 1974.
31. Ruus, R.; Kikas, A.; Saar, A.; Ausmees, A.; Nommiste, E.; Aarik, J.; Aidla, A.; Uustare, T.; Martinson, I. Ti 2p and O 1s X-ray absorption of TiO₂ polymorphs. *Solid State Commun.* **1997**, *104*, 199–203. [[CrossRef](#)]
32. Kucheyev, S.O.; Sadigh, B.; Baumann, T.F.; Wang, Y.M.; Felter, T.E.; Van Buuren, T.; Gash, A.E.; Satcher, J.H., Jr.; Hamza, A.V. Electronic structure of chromia aerogels from soft X-ray absorption spectroscopy. *J. Appl. Phys.* **2007**, *101*, 124315. [[CrossRef](#)]
33. Schedel-Niedrig, T.; Neisius, T.; Simmons, C.T.; Köhler, K. X-ray absorption spectroscopy of small chromium oxide particles (Cr₂O₃, CrO₂) supported on titanium dioxide. *Langmuir* **1996**, *12*, 6377–6381.
34. Dedkov, Y.S.; Vinogradov, A.S.; Fonin, M.; König, C.; Vyalikh, D.V.; Preobrajenski, A.B.; Krasnikov, S.A.; Kleimenov, E.Y.; Nesterov, M.A.; Rüdiger, U.; et al. Correlations in the electronic structure of half-metallic ferromagnetic CrO₂ films: An X-ray absorption and resonant photoemission spectroscopy study. *Phys. Rev. B* **2005**, *72*, 060401(R). [[CrossRef](#)]
35. Gago, R.; Vinnichenko, M.; Hübner, R.; Redondo-Cubero, A. Bonding structure and morphology of chromium oxide films grown by pulsed-DC reactive magnetron sputter deposition. *J. Alloy Compd.* **2016**, *672*, 529–535. [[CrossRef](#)]

